Available online at www.sciencedirect.com
SCIENCE DIRECT®
ELSEVIER
Nuclear Instruments and Methods in Physics Research A 551 (2005) 540–552
NUCLEAR INSTRUMENTS & METHODS IN PHYSICS RESEARCH Section A
www.elsevier.com/locate/nima

Novel scatter correction for three-dimensional positron emission tomography by use of a beam stopper device

Keh-Shih Chuang[a,*], Jay Wu[a,b], Meei-Ling Jan[a,c], Sharon Chen[a], Ching-Han Hsu[a]

[a]*Department of Nuclear Science, National Tsing-Hua University, 101, Sec. 2, Guangfu Rd., Hsinchu 30013, Taiwan*
[b]*Health Physics Division, Institute of Nuclear Energy Research, Atomic Energy Council, Taiwan*
[c]*Physics Division, Institute of Nuclear Energy Research, Atomic Energy Council, Taiwan*

Received 15 December 2004; received in revised form 13 May 2005; accepted 9 June 2005
Available online 12 July 2005

Abstract

Modern positron emission tomography scanners generally perform three-dimensional data collection without septa, which increases not only true coincidences but also scattered coincidences. In this study, a beam stopper (BS) device which is made of lead was used to estimate the scatter component in the PET sinogram. Scattered events were then directly measured from those lines of response blocked by stoppers. By assuming that the scatter distribution is a spatially slow-varying function, the scatter component can be recovered using the cubic-spline interpolation from the local measurements. Monte Carlo simulations of an abdomen phantom and the Zubal phantom were performed. Preliminary results demonstrated that the proposed BS method can improve image contrast and quantitative accuracy. Among different configurations, the BS device consisting of twelve lead stoppers with 3 mm radius yielded the optimal result compared to the other BS configurations. This BS method also outperformed the dual-energy window method up to 40% based on the mean squared error. The results indicated that the proposed BS method permits a direct, fast, and accurate scatter correction.

PACS: 87.58.Fg

Keywords: Beam stopper; Scatter correction; Positron emission tomography

1. Introduction

Positron emission tomography (PET) is a powerful diagnostic tool for oncology, due to its high sensitivity and specificity for detecting a variety of cancers. PET is also an enable

*Corresponding author. Tel.: +886 3 574 2681; fax: +886 3 571 8649.
E-mail address: kschuang@mx.nthu.edu.tw (K.-S. Chuang).

0168-9002/$ - see front matter © 2005 Published by Elsevier B.V.
doi:10.1016/j.nima.2005.06.050

technology to quantify the activity distribution of radionuclides in vivo. However, scattered events in PET would reduce image contrast and inevitably lead to an overestimation of actual activity distribution. To achieve accurate quantification, adequate scatter correction is essential in PET.

Accurate scatter correction is a challenging task. For fully three-dimensional (3D) PET, the septa used to reject interplane scattered events are retracted in order to increase the sensitivity [1]. The corresponding scatter fraction usually occupies about 14–36% of the total detected coincident events in the brain study [2], and even markedly constitutes over 50% in the human thorax case [3]. The estimation of the scatter component depends on many physical parameters including energy resolution of detectors, energy window settings of a scanner, radionuclide source distribution, and sizes and materials of an object. These parameters are often non-stationary, and impose a potential difficulty when designing appropriate scatter correction techniques.

Rejection of scattered events based on energy discrimination has limited success, owing to the poor energy resolution of the scintillator [4,5]. There are also other correction methods that are based on energy windows, curve fitting, convolution subtraction, model-based, and reconstruction-based approaches [6–9]. These methods merely differ in the way they estimate the scatter component.

Multiple energy window methods have previously been proposed for single photon emission computed tomography (SPECT) [10–12]. Recent developments and improvements in energy resolution of PET detectors have enabled the implementation of scatter correction based on energy spectra [13–15]. These methods assume that the high energy (photopeak) window contains both primary and scattered events, while the low energy window mainly contains scattered events. The amount of scattered radiation in both windows is associated with a scatter ratio, which is assumed to be a constant. The scattered events can be estimated and corrected through a linear combination of the two data sets from both windows. Since the scatter ratio varies with the attenuation coefficient and the source distribution, these methods may not adequately handle large or non-uniform objects.

The curve fitting techniques [16] are based on the assumption that the spatial distribution of scatter can be described through a Gaussian function or second-order polynomials. The center of the scatter distribution is interpolated from the region outside the source object. The assumption may be invalid for scanning of the human torso, which is large and not homogeneous. Using a similar scheme, Cherry and Huang compared 2D and 3D scans to estimate the scatter contamination [17]. However, this method requires an additional 2D scan, which could be impractical for clinical use.

Convolution subtraction approaches [18–20] estimate the scatter distribution based on standard photopeak data. These methods use constant scatter kernels, which are parameterized via mono-exponential or Gaussian functions. The scatter distribution is then estimated by iteratively convolving the photopeak projections with the kernel. However, these techniques do not consider the scattered events originating from outside the field of view (FOV). And the kernels are usually measured by using simple phantoms that might not adequately represent human anatomy.

Model-based approaches [3,21–28] estimate the scatter component relying on a rigorous analytical modeling based on the underlying physics of Compton scattering. The single-scatter simulation (SSS) algorithm proposed by Watson et al [3,21] calculates the single scatter distribution by using emission and transmission data. Recently, a new implementation of SSS [28] requires less than 5 min execution time for a whole-body study. Ollinger [25] incorporated the multiple scatter as an integral transformation of the single scatter distribution. In reconstruction-based methods, Werling [27] optimized the implementation of the SSS algorithm, which resulted in a significant speedup of the scatter estimation procedure. The scatter simulation was then included in the forward projection step of maximum likelihood image reconstruction. These methods work very well when dealing with single scattering. However, they still share a common disadvantage in handling scattered events outside the FOV [26].

In seeking an alternative, we proposed a beam stopper (BS) device, which has been widely applied to measure scatter in radiography [29]. The proposed BS device consists of several lead rods and is designed to directly measure scattered events. The purpose is to extend the use of the device to develop a reliable scatter correction scheme for PET, with the aim of accurately estimating and eliminating scatter from the reconstructed images.

2. Methods

2.1. Beam stopper

A beam stopper made of high Z material was used to measure the scatter component. It was installed in front of a detector to block true (primary) events from being recorded. To minimize its influence on scattered events, the size of a stopper should be small and the location should be placed as close to the object as possible (Fig. 1). For each projection angle θ with respect to the x-axis, the stopper interacted mainly with the primary events emitted from the sources along the specific line of response (LOR)

$$x_i \cos\theta + y_i \sin\theta = t_i \tag{1}$$

where (x_i, y_i) indicates the location of the ith stopper in space. Depending on the material and size of the stopper, a transmission fraction ($T \leqslant 1$) of the primary events would penetrate through the stopper and be recorded by the detector. Suppose that S and P be the scatter (from inside and outside the FOV) and primary components from the original source, respectively. Let C_B and C_R be the counts at a given LOR in the sinogram with and without the stopper, respectively. Then, we can write C_B and C_R as

$$C_R(t_i, \theta) = P(t_i, \theta) + S(t_i, \theta) \tag{2}$$

$$C_B(t_i, \theta) = T(t_i, \theta) \times P(t_i, \theta) + S(t_i, \theta) \tag{3}$$

P and S for each detector pair (t_i, θ) can be solved, once the transmission fraction $T(t_i, \theta)$ is obtained by the air scan. Note that T will be equal to 1 for those LORs that do not intersect with the beam stopper.

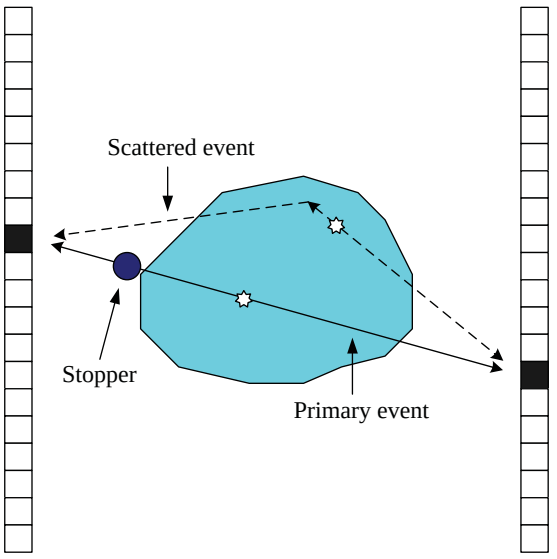

Fig. 1. The geometry of the system with single beam stopper. For each projection angle θ, the stopper interacted mainly with the primary events emitted from sources along on the specific LOR.

2.2. Air scan

In the air scan, a point source was moved around and spent the same period of time at each location inside the FOV. Let C_{B0} and C_{R0} denote the counts for the air scans with and without the beam stopper device, respectively. The corresponding transmission fraction T is simply the ratio of these estimates as shown in Eq. (4)

$$T(t, \theta) = C_{B0}(t, \theta)/C_{R0}(t, \theta) \tag{4}$$

The air scans need to be performed only once for the specific arrangement of a beam stopper device. Information on T was then stored for the subsequent object scans.

2.3. Scatter component

The scatter component at the LOR corresponding to the beam stopper was obtained by solving Eqs. (2) and (3) to yield Eq. (5)

$$S(t_i, \theta) = \frac{\mathrm{Med}\{C_B(t_i, \theta)\} - T(t_i, \theta) \times \mathrm{Med}\{C_R(t_i, \theta)\}}{1 - T(t_i, \theta)} \tag{5}$$

where Med(·) denotes a 5×5 median filter to remove noise from the projection data. Due to the finite size of the beam stopper, the transmission fractions at several neighboring locations of t_i were not constant. Consequently, for each stopper, the scatter component was estimated from the location t_i where its transmission fraction has the minimal ratio.

2.4. Multiple beam stoppers

A device consisting of multiple beam stoppers was placed surrounding an object to achieve multiple readings of the scatter component. For a given projection angle, the primary events were blocked at several radial bins (Fig. 2a). The scatter component was then estimated at these bins, where T values were local minima. Since the scatter distribution was assumed to be a spatially slow-varying function, the entire distribution was recovered through the cubic-spline interpolation from the values calculated at the stopper locations (Fig. 2b). Finally, the whole scatter sinogram was smoothed using a 7×7 Gaussian filter.

2.5. Primary component

The object scan was divided into two sub-scans, one in the presence of the beam stopper device and one in its absence. Both data sets were used to calculate the primary sinograms

$$P_R(t,\theta) = C_R(t,\theta) - S(t,\theta) \tag{6}$$

$$P_B(t,\theta) = \frac{C_B(t,\theta) - S(t,\theta)}{T(t,\theta)} \tag{7}$$

These two primary sinograms were summed together for primary image reconstruction. Therefore, no additional scanning time for the object is required.

2.6. Validation through monte carlo simulations of digital phantoms

The validation was performed using Monte Carlo code of the Simulation System for Emission Tomography (SimSET) from the University of Washington [30]. The scattered and unscattered events were distinguished from each other and

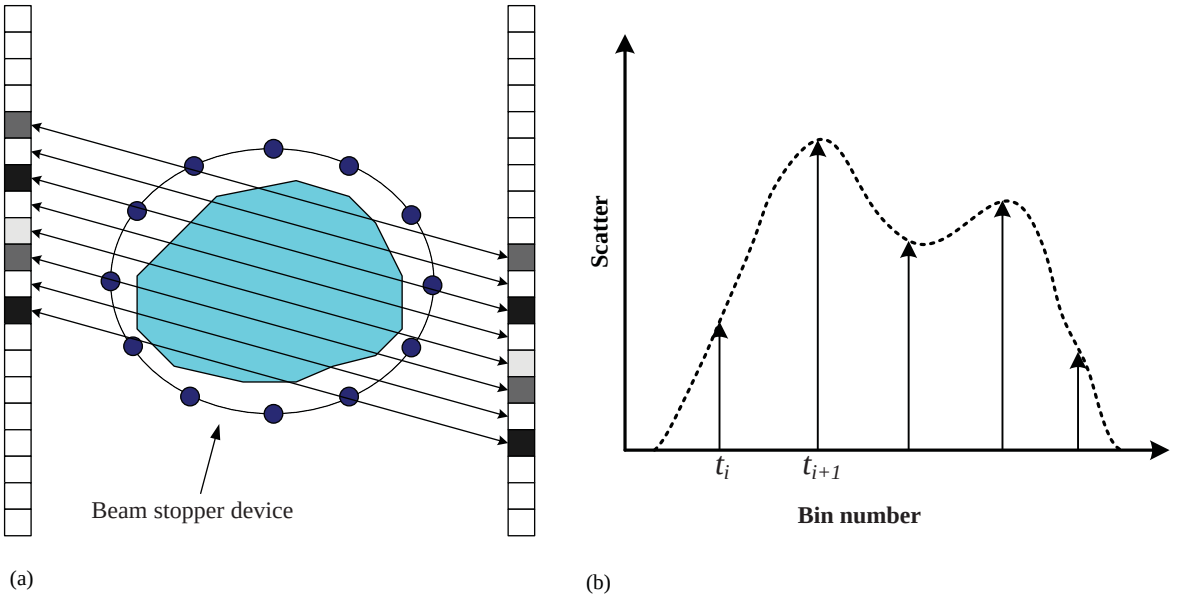

Fig. 2. (a) For each projection angle, the primary events were blocked at several radial bins. (b) The scatter distribution (dotted line) was interpolated based on the scatter components (solid arrow) estimated at those blocked bins where the transmission fractions were local minima.

binned into separate sinograms as a gold standard for the comparison.

Fig. 3 shows the geometry of the simulated abdomen phantom [31] and the setting of the beam stopper device under study. Four cylindrical sources (regions A, B, C, and D with respective radii of 0.625, 0.935, 1.25, and 5 cm) were inserted into an elliptical cylinder with a long axis of 34 cm and a short axis of 26 cm. The phantom and the sources were 20 cm long to include scattered events from activity outside the axial FOV. The four hot regions and background were water-filled with activity concentrations equal to 37 MBq/cc and 5.5 MBq/cc, respectively. A cold spot (region E with a radius of 1.563 cm) was inserted inside the largest cylinder. The beam stopper device was designed as a birdcage with a radius of 18.5 cm, consisting of 12 lead rods (radius $r = 0.3$ cm) arranged uniformly on the surface.

An anthropomorphic Zubal phantom [32] was constructed for performance evaluation as well. Three types of tissues including lung, blood pool, and soft tissue were filled with activity concentrations of 3.7, 37, and 18.5 MBq/cc, respectively. The phantom was then rescaled to long and short axes of approximately 32 and 18 cm, respectively, to fit into the beam stopper device, which consisted of twelve three-mm-radius stoppers.

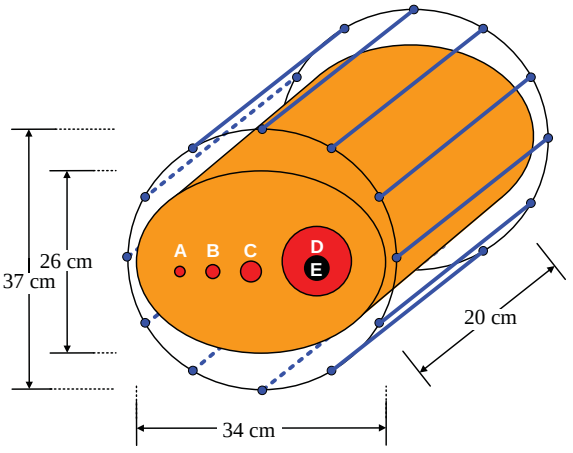

Fig. 3. The elliptical abdomen phantom inserted with four cylinders (regions A, B, C, and D from left to right) was used for the simulation study. The activity concentrations in the cylinders and background were 37 MBq/cc and 5.5 MBq/cc. A cold spot (region E) with no radioactivity was located inside the largest cylinder. Twelve beam stoppers were arranged uniformly around the phantom with a radius of 18.5 cm.

The PET system was simulated with a ring diameter of 80 cm and a transaxial FOV of 58 cm. The energy resolution of the detectors was about 20% at 511 keV and the spatial resolution was 0.33 × 0.33 cm^2. Since photon transport was not simulated in the detectors, all impinging photons were absorbed without any scattering inside the crystals, and no pile-up events occurred. The energy window of the primary photopeak was set at [380, 850] keV. There were total 180 angular projection samples, while each projection had 180 radial bins with bin size equal to 0.32 cm.The total numbers of traced decay were 2.0×10^{10} and 1.0×10^{9} for the air and object scans, respectively. The acquisition time was set to 60 s. The air scan was simulated using a cylindrical phantom filled with radioactive gas. It was expected that no Compton scattering occurs.

Attenuation correction was performed after scatter compensation, based on a prior knowledge of the geometric structure of the phantom and appropriate attenuation coefficients. The scatter-free image was reconstructed from the primary sinogram using the maximum-likelihood expectation-maximization (ML-EM) algorithm [33]. Following 100 iterations, a 5×5 median filter was applied to the final image.

2.7. Image quality assessment

The contrast (CS), mean squared error (MSE), and normalized standard deviation (NSD) were calculated for the reconstructed images to assess the performance of scatter compensation. The CS is defined by:

$$\mathrm{CS} = \frac{|l - b|}{l + b} \tag{8}$$

where l denotes the average activity in the region of interest (ROI) and b represents the average activity in the surrounding region. The contrast improvement was used to verify the scatter correction efficiency. The MSE is the mean of the squared activity differences between the reconstructed image and the digital phantom. It measures the accuracy of the scatter correction

method. Moreover, the NSD is the ratio of the standard deviation to the average activity measured in the background. It represents the noise level in the image results.

2.8. Dual-energy window method

Scatter correction using the dual-energy window (DEW) method was compared. In the DEW method [13], counts were simultaneously accumulated in the photopeak window [380, 850] keV and the Compton window [200, 380] keV. The scatter ratio R_{sc} is the ratio of the scatter contribution between two windows. This value varies with different planes. It was estimated by Monte Carlo simulation of a line source in an 18.5 cm radius water-filled cylinder with a length of 20 cm.The value of R_{sc} was equal to 0.22 for the central sinogram. The unscattered ratio R_{unsc} was zero because the energy of arriving photons was fully deposited in the detector. The total number of traced decay in the DEW method was the same as that in the BS method.

3. Results

Fig. 4 illustrates the sinograms of the air scan (C_{R0}), the air scan with the beam stopper device in place (C_{B0}), and the inverse of the transmission fraction ($1/T$). Each curve represents the ray integral of a stopper. The number of these curves through a profile was less than the number of stoppers because some projected positions of stoppers had no intersection with the phantom and some of them overlapped with each other.

Fig. 5 depicts a plot of the sinogram profiles of the phantom at $\theta = 36^\circ$ for C_R, C_B, and the calculated scatter distribution using various methods. The scatter components estimated at the blocked LORs are also shown as spikes. Some of the spikes were eliminated because a criterion that C_B must be larger than $T \times C_R$ was added to the calculating procedure to avoid negative values of scatter induced by statistical fluctuations. Clearly, the scatter distribution estimated by the BS method provided accuracy in shape and amplitude compared with the true scatter distribution by the Monte Carlo simulation. The profile achieved by the DEW method overestimated the counts near the edge because of using a constant scatter ratio throughout the object.

Fig. 6 displays the true scatter sinogram by the Monte Carlo simulation and the calculated scatter sinogram by the BS method, which are in a good agreement. Fig. 7 shows the reconstructed images from the original sinogram, primary sinogram by the BS method, and primary sinogram by the DEW method, respectively. Both scatter correction methods reduced the contamination of activity in the background. Significantly improved contrast and uniformity between the hot spots were prominent by using the BS method (Fig. 7c).

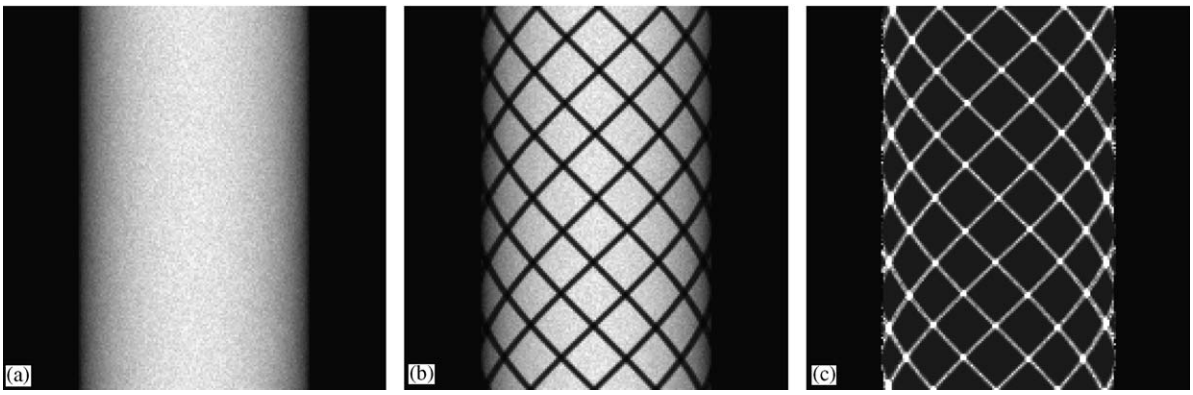

Fig. 4. The sinograms of (a) the air scan (C_{R0}), (b) the air scan with 12 beam stoppers in place (C_{B0}), and (c) the inverse of transmission fraction ($1/T$).

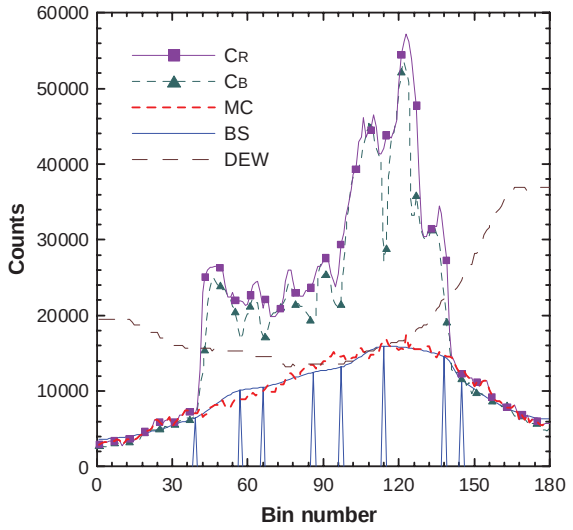

Fig. 5. The projected profiles of the phantom at $\theta = 36^\circ$ with and without the beam stopper device (C_B: triangles, C_R: squares, respectively). The scatter distributions estimated by the BS (solid), DEW (dashed), and Monte Carlo simulation (dotted) are shown. The spikes under the BS curve are the scatter components directly measured by the beam stoppers

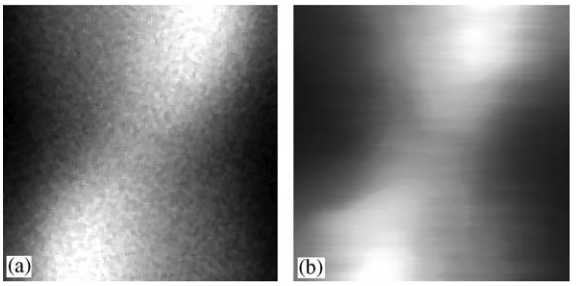

Fig. 6. The scatter sinograms estimated by (a) the Monte Carlo simulation and (b) the BS method.

Horizontal profiles through the center of the images before and after correction are compared in Fig. 8. The residual activity in the region E was smaller by the BS method, indicating that the removal of the scatter component was more efficient. The background activity between regions A and B was underestimated by the DEW method. This resulted from the over-estimation of the scatter component near the edge of the phantom. The activity concentration in region A was significantly lower than the activity in the phantom, probably because of the limitation of detector resolution and the smooth filter applied to the final image.

Table 1 compares the cold spot (region E) CS, MSE, and NSD obtained using the BS and the DEW methods. Twelve stoppers were arranged in the beam stopper device. We also investigated the performance with stopper radii varying from 0.3 upto 1.2 cm. The BS method improved the CS and MSE by approximately 10% and 40%, respectively, when compared to the DEW method. The noise induced by the BS method almost remained the same as in the original image. On the other hand, the noise induced by the DEW technique was more than double. This phenomenon was caused by the counting statistics in the low energy window being much noisier than the photopeak window, so that the subtraction procedure increased the noise level in the reconstructed images.

The comparison of stopper thicknesses showed that the 0.3 cm radius resulted in the best result for the 3 metrics considered. As the stopper size increased, the photon counts transmitted through the stopper exponentially decreased and the fluctuation in P_B (Eq. (7)) increased. Therefore, we might be able to exclude the P_B sinogram. For example, using P_R alone for 1.2-cm-radius stoppers produced a better reconstructed image quality, as compared to the use of both P_B and P_R under the same conditions.

Table 2 lists the contrasts measured in the four hot cylinders using the DEW and BS methods with various stopper sizes. The BS method with the 0.3 cm radius produced more accurate results in terms of restoring the true contrast. Due to the over-estimation of the scatter component by the DEW method, the CSs in regions A and B were extremely high. Although this should not influence a lesion detection task, it would introduce substantial errors in quantitative analysis. As the stopper size increased, the mean value deteriorated markedly. This is probably due to the fact that increasing the stopper size led to blocking more additional scattered events. Consequently, the scatter component was underestimated.

Various numbers of stoppers ($r = 0.3$ cm) were employed in the simulation of the same phantom to

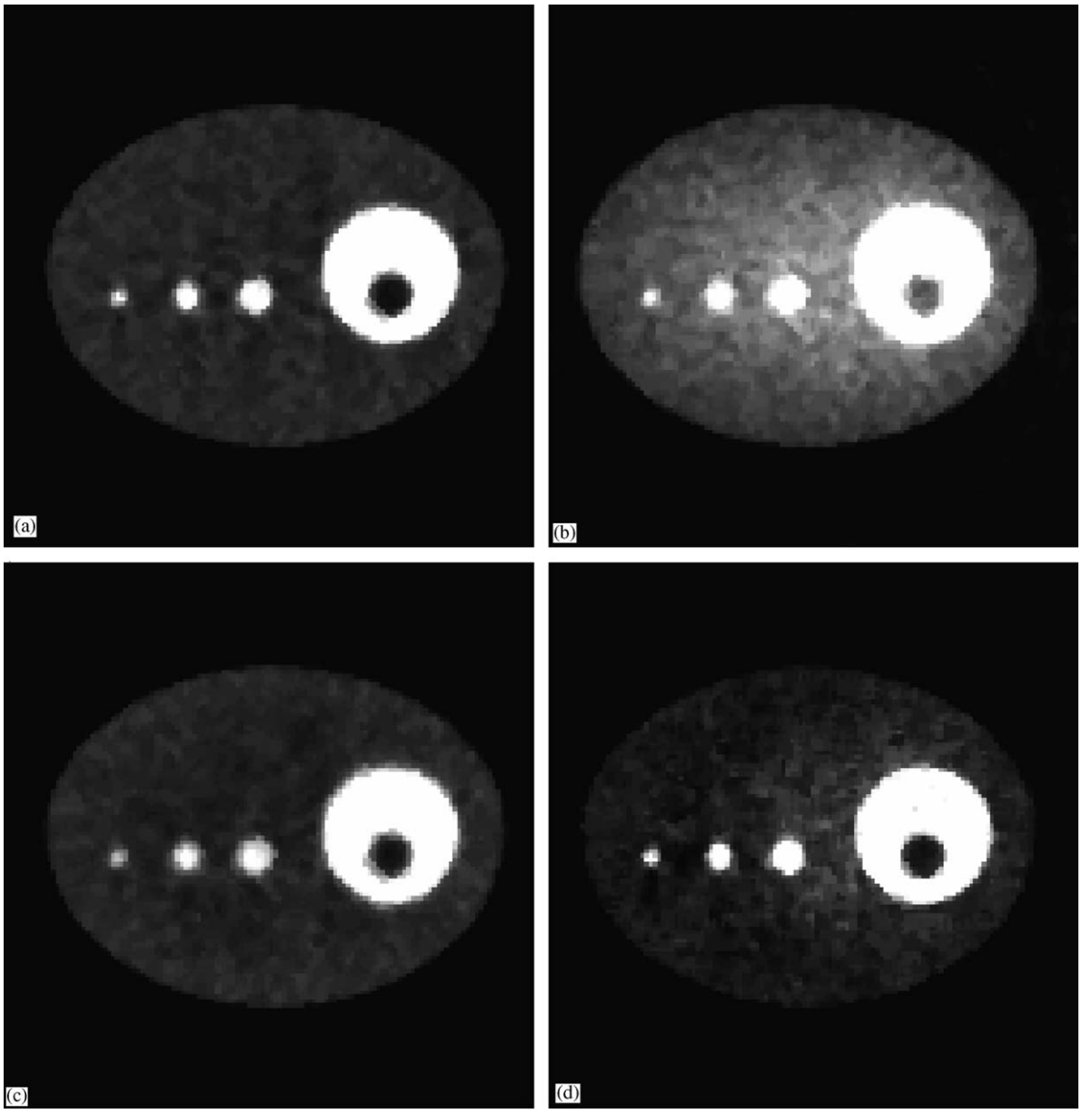

Fig. 7. The reconstructed images of the abdomen phantom. (a) The true unscattered image, (b) uncorrected image, (c) image corrected by the BS method, and (d) corrected by the DEW method.

determine the reasonable stopper number for abdomen scans. The contrasts of the cylindrical sources are tabulated in Table 3. Except for the stopper number $N = 4$, the CSs and other indices were similar. This means the image quality was saturated approximately at $N = 8$. Further increases in the number of stoppers would not provide more information on interpolation of the whole scatter distribution. As the stopper number reached 16, there was no further decrease in MSE. For a more complex object, the required number of stoppers might be larger, according to its size and composition.

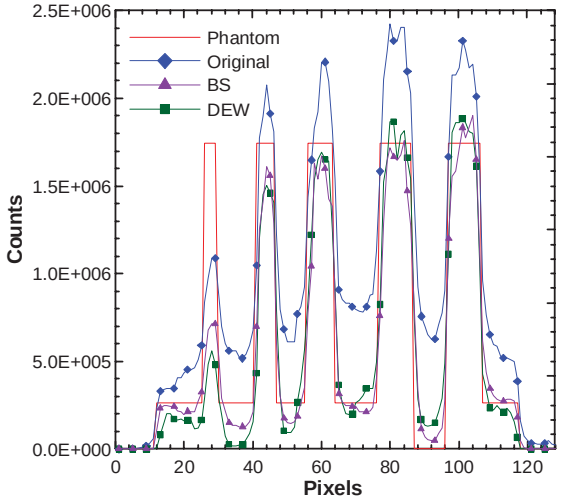

Fig. 8. The central horizontal profiles of the abdomen phantom (plain line), original image (diamonds), image corrected by the BS method (triangles), and image corrected by the DEW method (squares).

Table 1
Cold spot contrast (CS), mean squared error (MSE), and normalized standard deviation (NSD) of the abdomen phantom obtained by the DEW method and the BS method with stopper radii ranging from 0.3 to 1.2 cm

Method	CS (region E)	MSE ($\times 10^{10}$)	NSD
Phantom	1	—	—
Uncorrected	0.560±0.008	8.090	0.283
DEW	0.846±0.013	2.540	0.639
BS ($r = 0.3$ cm)	0.917±0.012	1.474	0.284
BS ($r = 0.6$ cm)	0.873±0.013	1.537	0.286
BS ($r = 0.9$ cm)	0.857±0.021	2.007	0.374
BS ($r = 1.2$ cm)	0.612±0.155	178.0	1.809
BS ($r = 1.2$ cm)*	0.638±0.087	9.470	0.851

*Only P_R was used for image reconstruction.

The reconstructed thorax images of the Zubal phantom before and after applying scatter correction are illustrated in Fig. 9. The BS method substantially reduced the residual activity in both lungs and raised the contrast between the blood pool and the myocardium. The horizontal profiles through the center of the images are plotted in Fig. 10. It is obvious that the BS-SF method accurately recovered the activity concentrations of different regions. It also restored the average

Table 2
Hot spot contrasts of the abdomen phantom measured in the four hot cylinders by the DEW method and the BS method with stopper radii ranging from 0.3 to 1.2 cm

Method	CS (region)				Mean (±SD)
	A	B	C	D	
Phantom	0.739	0.739	0.739	0.739	0.739
Uncorreted	0.381	0.408	0.436	0.464	0.422±0.04
DEW	0.818	0.827	0.752	0.745	0.785±0.04
BS ($r = 0.3$ cm)	0.724	0.754	0.738	0.746	0.741±0.01
BS ($r = 0.6$ cm)	0.715	0.733	0.737	0.728	0.728±0.01
BS ($r = 0.9$ cm)	0.495	0.642	0.645	0.687	0.617±0.08
BS ($r = 1.2$ cm)	0.826	0.743	0.263	0.548	0.595±0.25
BS ($r = 1.2$ cm)*	0.456	0.419	0.534	0.637	0.511±0.10

*Only P_R was used for image reconstruction.

Table 3
Contrasts of the abdomen phantom measured in the four hot cylinders using the BS method with various numbers of stoppers ranging from 4 to 16 ($r = 0.3$ cm)

Number of stoppers	CS (region)				MSE ($\times 10^{10}$)	NSD
	A	B	C	D		
Phantom	0.739	0.739	0.739	0.739	—	—
4	0.686	0.710	0.696	0.712	1.442	0.272
8	0.722	0.757	0.737	0.745	1.487	0.302
12	0.724	0.754	0.738	0.746	1.474	0.284
16	0.727	0.755	0.740	0.745	1.499	0.284

activity ratio of the soft tissue/lung from 1.75 to 5.20 (ideal value of 5.0) and the ratio of the blood pool/lung from 3.25 to 9.81 (ideal value of 10.0). Table 4 summarizes the comparisons of quality indices before and after correction. A hot region in the blood pool, a cold region in the left lung, and a background in the right lung were used to calculate the CS and NSD. The data again show the encouraging results that the BS method markedly improved the CS and MSE without increasing NSD.

4. Discussion

This research attempted to compensate scatter contamination using a beam stopper device. By

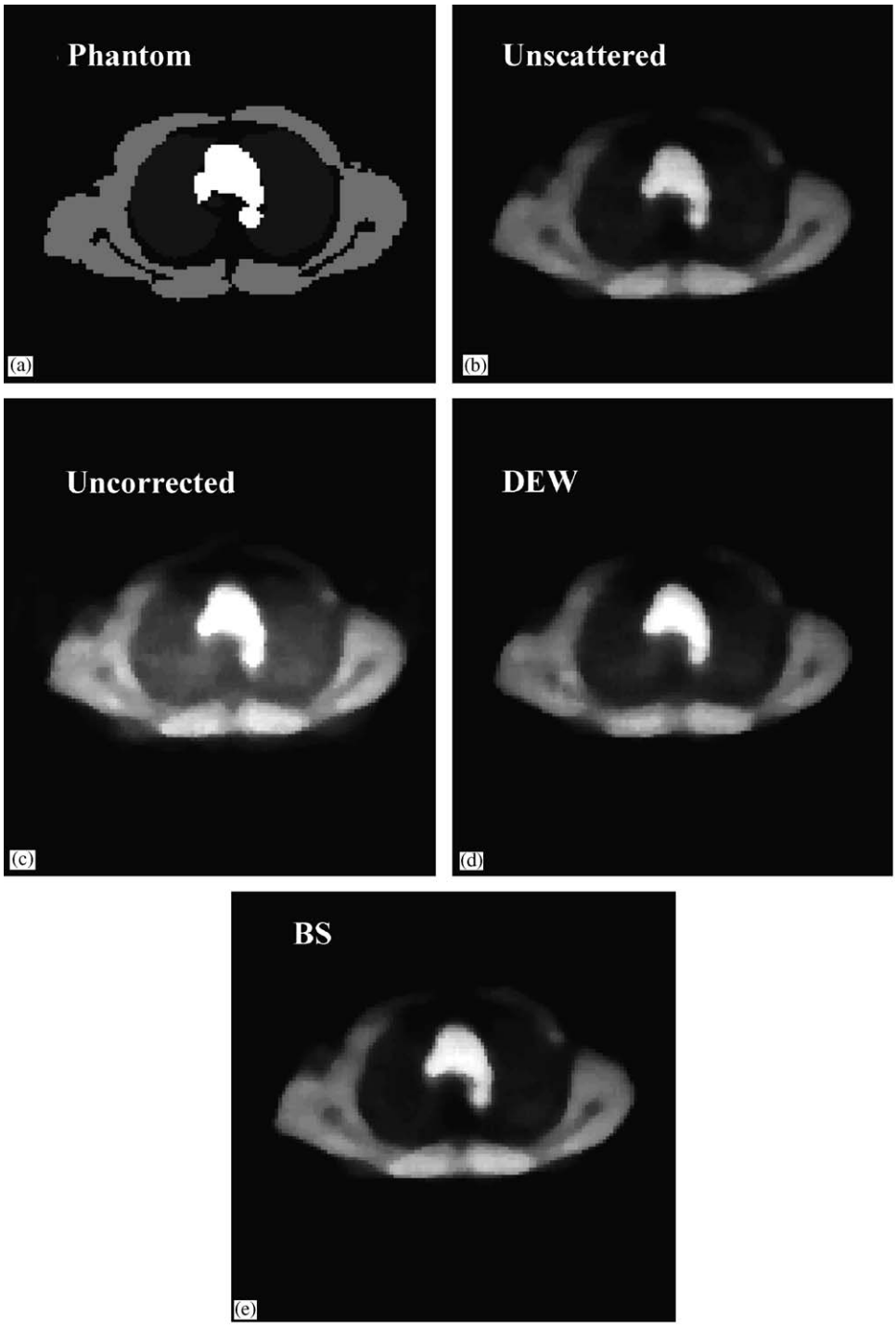

Fig. 9. The reconstructed images of the Zubal phantom. (a) The reference image used as input to the simulator, (b) the true unscattered image, (c) uncorrected image, (d) image corrected by the DEW method, and (e) corrected by the BS method.

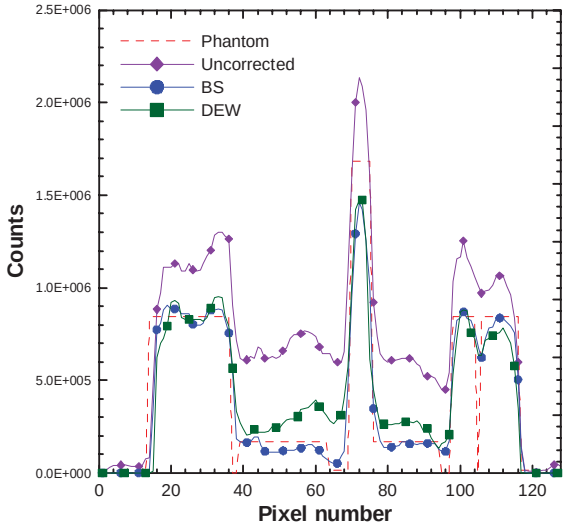

Fig. 10. The horizontal profiles through the center of the reconstructed images before and after applying the BS-SF and DEW methods.

Table 4
Contrast (*CS*), mean squared error (*MSE*), and normalized standard deviation (*NSD*) of the Zubal phantom obtained by the DEW method and the BS method

Method	CS	MSE ($\times 10^{10}$)	NSD
Phantom	0.780	—	—
Uncorreted	0.432	6.307	0.302
DEW	0.657	3.701	0.463
BS	0.849	2.373	0.332

assuming scattered radiation to be a spatially slow-varying function, the estimated scatter distribution perfectly matched the distribution obtained by the Monte Carlo simulation. But, for some complicated objects, this assumption may not be true. If we increase the number of stoppers, the scatter component between stoppers would more likely fit with a low order function. The interpolation approach can then well portrait the true scatter distribution. Since the cubic spline is used to restore the scatter distribution, the positions of stoppers will determine where the scatter components are measured. The most suitable arrangement of stoppers would be the uniform distribution around a patient.

Beam stoppers also have unavoidable impact on scattered events. For example, in the Monte Carlo study of Zubal phantom, there are approximately 5% scattered events attenuated by stoppers. This additional attenuation on scatter currently cannot be taken into account by the BS method. Fortunately, thinner stoppers can be implemented in practice, as long as the corresponding attenuation fraction of primary events is distinguishable from the Poisson error. A tradeoff between stopper number/radius configurations, therefore, should be made to optimize the performance for various scanning conditions.

For a practical implementation of the BS method, the lead bars could be assembled as a half birdcage shown in Fig. 11. This structure can be easily attached to and removed from a patient between two sub-scans. There is no need to have the beam stoppers surrounding the patient to block both annihilation photons, as the coincidence circuit works with one side being blocked. The transmission fraction for each LOR can be determined from the dual blank scans with and without the beam stopper device, using an external transmission source such as ^{68}Ge.

For real scanner systems, a minimum amount of time is required between successive events to resolve them as two separate counts. This minimum time separation is called the dead time of the counting system. A true event will be lost if it occurs too quickly following the preceding event.

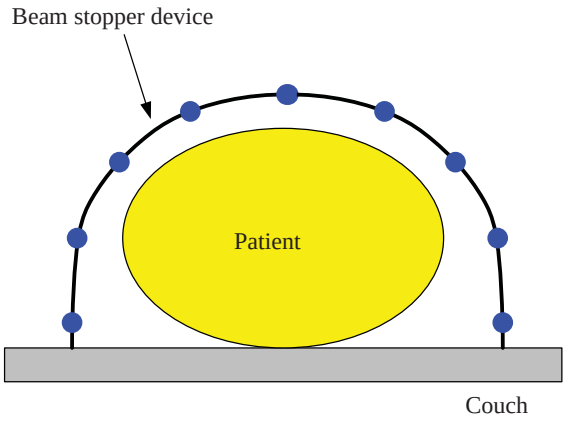

Fig. 11. The beam stopper device could be designed as a half cylindrical birdcage.

In the proposed method, the air scan can be performed using a low activity transmission source to minimize the dead time effect. In the object scan, the count rates between the two sub-scans with and without the beam stopper device are different and the dead time loss can vary considerably. This leads to an over-estimation of the scatter component. To circumvent this problem, the dead time correction [7] on the sinogram must be performed before the scatter correction.

The random coincidence is another important component constituting the total coincidences. Its distribution in the sinogram tends to be a fairly slowly changing function [7], which is similar to the scatter distribution. Besides, if the stopper is small, the random coincidence can also fulfill the assumption that the beam stopper device has no impact on it. Therefore, we believe that random events can be considered together with scattered events. In fact, Karp et al (1990) [34] used the tail fitting technique to correct them together. Since the current version of SimSET does not implement the random simulation, this study only addresses the scatter component.

Some other scatter correction methods available on clinical scanners perform well in both 2D and 3D systems, like model-based methods [3,21]. These methods have several disadvantages. Firstly, the computation is very demanding if the volume is integrated over every possible scattering point. Secondly, the scatter arising from activity outside the axial FOV must be approximated. Thirdly, implementation is complex. In contrast, the proposed BS method measures scattered coincidences directly from inside and outside the FOV, works for single and multiple scatter in the direct and oblique planes, is simple to implement, and provides fast data processing.

5. Conclusions

This study has proposed an accurate scatter correction method employing the beam stopper device. It is a fast and simple technique based on the direct measurement of scattered events coming from inside and outside the FOV. Preliminary results indicate that the BS method accurately estimates the scatter distribution's shape and amplitude without using a scaling factor. The BS method outperforms the DEW method in contrast recovery, noise reduction, and accuracy. We suggest that the installation the beam stopper device with twelve 3-mm-radius lead stoppers should be the optimal choice for abdomen scans. The technique is amenable to corrections of multiple scatter and scatter contributed from activity outside the field of view.

Acknowledgements

The authors would like to thank the National Science Council of Taiwan for financially supporting this research under Contract No. NSC93-2314-B-007-002 and NSC93-2623-7-007-015-NUSC. is supported by a research grant from the Institute of Nuclear Energy Research, Taiwan.

References

[1] D.W. Townsend, A. Geissbuhler, M. Defrise, E.J. Hoffman, T.J. Spinks, D.L. Bailey, M.C. Gilardi, IEEE Trans. Med. Imag. 10 (1991) 505.
[2] T.J. Spinks, T. Jones, D.L. Bailey, D.W. Townsend, S. Grootoonk, P.M. Bloomfield, M.C. Gilardi, M.E. Casey, B. Sipe, J. Reed, Phys. Med. Biol. 37 (1992) 1637.
[3] C.C. Watson, D. Newport, M.E. Casey, R.A. deKemp, R.S. Beanlands, M. Schmand, IEEE Trans. Nucl. Sci. 44 (1997) 90.
[4] A. Weisenberger, M. Williams, R. Wojcik, S. Majewski, F. Farzanpay, A. Goode, B. Kross, D. Steinbach, Nucl. Instr. and Meth. A 409 (1998) 520.
[5] B. Axelsson, P. Msaki, A. Israelsson, J. Nucl. Med. 25 (1984) 490.
[6] H. Zaidi, Eur. J. Nucl. Med. 27 (2000) 1813.
[7] S.R. Meikle, R.D. Badawi, Quantitative techniques in Positron Emission Tomography, in: P.E. Valk, D.L. Bailey, D.W. Townsend, et al. (Eds.), Positron Emission Tomography: Basic Science and Clinical Practice, Springer, London, 2003, pp. 115–146.
[8] H. Zaidi, K.F. Koral, Eur. J. Nucl. Med. Mol. Imag. 31 (2004) 761.
[9] D.L. Bailey, et al., Quantitative procedures in 3D PET, in: B. Bendriem, D.W. Townsend (Eds.), The theory and practice of 3D PET, Kluwer Academic Publishers, The Netherlands, 1998, pp. 55–109.
[10] G. Loudos, N. Sakelios, N. Giokaris, K. Nikita, N. Uzunoglu, D. Maintas, Nucl. Instr. and Meth. A 527 (2004) 145.

[11] K.F. Koral, Y. Dewaraja, Nucl. Instr. and Meth. A 422 (1999) 688.
[12] J.Q. Luo, K.F. Koral, Nucl. Instr. and Meth. A 353 (1994) 340.
[13] S. Grootoonk, T.J. Spinks, D. Sashin, N.M. Spryou, T. Jones, Phys. Med. Biol. 41 (1996) 2757.
[14] L. Shao, R. Freifelder, J.S. Karp, IEEE Trans. Med. Imag. 13 (1994) 641.
[15] R.J. Jaszczak, K.L. Greer, C.E. Floyd, C.C. Harris, R.E. Coleman, J. Nucl. Med. 25 (1984) 893.
[16] S.R. Cherry, S.R. Meikle, E.J. Hoffman, J. Nucl. Med. 34 (1993) 671.
[17] S.R. Cherry, S.C. Huang, IEEE Trans. Nucl. Sci. 42 (1995) 1174.
[18] M. Bentourkia, P. Msaki, J. Cadorette, R. Lecompte, J. Nucl. Med. 36 (1995) 121.
[19] B.T.A. Mckee, A.T. Gurvey, P.J. Harvey, D.C. Howse, IEEE Trans. Med. Imag. 11 (1992) 560.
[20] D.L. Bailey, S.R. Meikle, Phys. Med. Biol. 39 (1994) 411.
[21] C.C. Watson, IEEE Trans. Nucl. Sci. 47 (2000) 1587.
[22] C.S. Levin, M. Dahlbom, E.J. Hoffman, IEEE Trans. Nucl. Sci. 42 (1995) 1181.
[23] D.J. Kadrmas, E.C. Frey, S.S. Karimi, B.M.W. Tsui, Phys. Med. Biol. 43 (1998) 857.
[24] S.D. Wollenweber, IEEE Trans. Nucl. Sci. 49 (2002) 722.
[25] J.M. Ollinger, Phys. Med. Biol. 41 (1996) 153.
[26] N.C. Ferreira, R. Trebossen, C. Lartizien, V. Brulon, P. Merceron, B. Bendriem, Phys. Med. Biol. 47 (2002) 1555.
[27] A. Werling, O. Bublitz, J. Doll, L.-E. Adam, G. Brix, Phys. Med. Biol. 47 (2002) 2947.
[28] R. Accorsi, L.-E. Adam, M.E. Werner, J.S. Karp, Phys. Med. Biol. 49 (2004) 2577.
[29] L.T. Niklason, J.A. Sorenson, J. Nelson, Med. Phys. 8 (1981) 677.
[30] R.L. Harrison, S.D. Vannoy, D.R. Haynor, S.B. Gillispie, M.S. Kaplan, T.K. Lewellen, Conf. Record, IEEE Nuclear Science Symp. (1993).
[31] C. Kamphuis, F.J. Beekman, P.P. van Rijk, M.A. Viergever, Eur. J. Nucl. Med. 25 (1998) 8.
[32] I.G. Zubal, C.R. Harrell, E.O. Smith, Z. Rattner, G. Gindi, P.B. Hoffer, Med. Phys. 21 (1994) 299.
[33] L.A. Shepp, Y. Vardi, IEEE Trans. Med. Imag. 1 (1982) 113.
[34] J.S. Karp, G. Muehllehner, D.A. Mankoff, C.E. Ordonez, J.M. Ollinger, M.E. Daube-Witherspoon, A.T. Haigh, J. Nucl. Med. 31 (1990) 617.